Acta Crystallographica Section A
Foundations of Crystallography
ISSN 0108-7673

Received 12 February 2001
Accepted 27 June 2001

Electron-density distribution in stishovite, SiO_2: a new high-energy synchrotron-radiation study

A. Kirfel,[a]* H.-G. Krane,[a] P. Blaha,[b] K. Schwarz[b] and T. Lippmann[c]

[a]Mineralogisch-Petrologisches Institut, Universität Bonn, Poppelsdorfer Schloss, D-53115 Bonn, Germany, [b]Institut für Physikalische und Theoretische Chemie, Technische Universität Wien, Getreidemarkt 9/156, A-1060 Wien, Austria, and [c]GKSS, Max-Planck-Strasse, D-21502 Geesthacht, Germany. Correspondence e-mail: kirfel@uni-bonn.de

The electron-density distribution of the high-pressure polymorph of SiO_2, stishovite [$a = 4.177$ (1) , $c = 2.6655$ (5) Å, space group $P4_2/mnm$, $Z = 2$], has been redetermined by single-crystal diffractometry using synchrotron radiation of 100.42 and 30.99 keV, respectively, in order to obtain essentially absorption- and extinction-free data. Room-temperature diffraction experiments on two samples of irregular shape were carried out on two different diffractometers installed at HASYLAB/DESY, Hamburg, Germany. The structure refinement on the high-energy data converged at $R(F) = 0.0047$, $wR(F) = 0.0038$, GoF = 0.78, for a multipole model with neutral atoms and multipole expansions up to seventh order. For each atom, the radial expansion coefficients of the multipole orders ($l > 0$) were constrained to a common value. The absence of extinction was indicated by a refined correction parameter equalling zero within error limit. The excellent quality of the data is also illustrated by a high-order (HO) refinement ($s > 0.7$ Å^{-1}) yielding $R(F) = 0.0060$, $wR(F) = 0.0048$, GoF = 0.85. Both static deformation electron-density distribution and structure amplitudes compare well with corresponding results obtained from band-structure calculations using the linearized-augmented-plane-wave (LAPW) method. Ensuing topological analysis of the total model electron density distribution revealed bond critical point properties for the two unique Si—O bonds, indicating a predominantly closed-shell interaction mixed with a significant shared interaction contribution that decreases with increasing interatomic distance. Calculation of atomic basins yielded charges of +3.39 e and −1.69 e for Si and O, respectively, in good agreement with the theoretically calculated values of +3.30 e and −1.65 e. The volumina of the Si and O basins are 2.32 and 10.48 Å^3, corresponding to spheres with radii of 0.82 and 1.36 Å, respectively. The results also conform well with correlations between bond length and bond critical point properties reported in the literature for geometry-optimized hydroxyacid molecules. Estimates of the Si cation electronegativity indicate that the change of Si coordination by oxygen from 4 to 6 is accompanied by an increase of the ionicity of the Si—O bond of about 7%.

1. Introduction

Stishovite is a high-pressure polymorph of silica and is one of the few non-metal dioxide members of the large group of oxides and fluorides crystallizing in the tetragonal rutile-type structure [space group no. 136, $P4_2/mnm$ (*International Tables for X-ray Crystallography*, 1974), $Z = 2$]. The first synthesis at high pressure and temperature was reported by Stishov & Popova (1961) followed by its discovery in an impact breccia at Meteor Crater, Arizona (Chao *et al.*, 1962). In contrast with all other known silica polymorphs which consist of corner-sharing SiO_4 tetrahedra, *i.e.* containing fourfold-coordinated Si, stishovite exhibits sixfold-coordinated Si and thus presents the unique opportunity to study the properties of elongated Si—O bonds in a small symmetric structure which is chemically simple and simultaneously highly relevant to the geophysics and mineralogy of the earth's mantle (Hill *et al.*, 1983). Although other structures containing sixfold-coordinated Si of hollandite- (Ringwood *et al.*, 1967; Reid & Ringwood, 1969), garnet- (Ringwood, 1967) and perovskite-type (Yagi *et al.*, 1978) are known, these structures are more complex and difficult to obtain, so that stishovite remains the most attractive candidate to be investigated. The small structure [$a = 4.177$ (1), $c = 2.6655$ (5) Å] consists of orthorhombically distorted SiO_6 octahedra which, by sharing opposite base edges, form continuous chains running along the [001] direc-

tion. Connection between the chains is achieved by corner sharing, giving rise to a planar threefold coordination of the O atom. Owing to the higher Si and O coordinations, as compared with the other silica polymorphs, and shorter distances between non-bonded O atoms, the density of stishovite (4.28 kg m^{-3}) exceeds that of the lower-pressure polymorph coesite by the remarkable amount of ∼46%. Fig. 1 shows the arrangements of both the coordination polyhedra and the bonds viewed approximately along the *c* axis. As indicated, there are two unique Si—O bonds: a longer axial one of length 1.809 (1) Å and a shorter equatorial one of length 1.757 (1) Å, which lies in the shared-edge plane (110). Compared with the mean bond length observed in SiO_4 tetrahedra, 1.626 Å (Gibbs, 1982), both bonds are about 10% longer. Since the Si cation on the inversion centre (2*a*; 0,0,0; *mmm*) is engaged in four equatorial and two axial bonds and the oxygen (4*f*; *x*,*x*,0; *mm*) correspondingly in one axial and two equatorial bonds, there are mainly two planes of interest for density mapping. The first runs through the SiO_6 polyhedron and contains two axial and two equatorial bonds, whereas the second is defined by the O atom and its next Si neighbours.

The first explicit electron-density-distribution study by conventional independent-atom-model (IAM) refinement, augmented by variation of the valence-shell populations, was reported by Hill *et al.* (1983). This analysis, based on 217 observed Mo $K\alpha$ data up to $s_{max} = (\sin\theta/\lambda)_{max} = 1.22$ Å^{-1}, yielded agreement indices $R(F) = 0.012$, $R_w(F) = 0.014$, GoF = 2.28, net atomic charges of +1.71 and −0.86 (15) e for Si and O, respectively, and deformation density accumulations of up to 0.47 and 0.29 e Å^{-3} on the shorter equatorial and longer axial bonds, respectively.

Since this work was, however, impeded by severe extinction affecting several low-order reflections (*e.g.* almost 50% for reflection 110), Spackman *et al.* (1987) (hereafter referred to as SHG) redetermined the density distribution using the same data, but replacing the 25 lowest-angle and extinction-affected structure amplitudes by corresponding data obtained from low-extinction powder diffraction measurements. Although some extinction still remained, this measure and the refinement with a generalized structure factor (GSF) model with multipoles of order $l = 1$ to $l = 4$ resulted in significantly improved agreement indices, $R(F) = 0.0077$, $R_w(F) = 0.0074$, GoF = 1.21, and ensuingly to an extensive density analysis by both Fourier and direct-space mapping, in particular of the dynamic and static deformation density distributions in the two planes addressed above. According to the models chosen, one with neutral atoms, the other with Si^{2+} and O^-, no formal charges were assessed. The obtained 'bond density' peaks on the Si—O bonds reached 0.27 e Å^{-3} on the short bond and 0.10 e Å^{-3} on the long one, values that, although being substantially smaller than those reported by Hill *et al.* (1983), reproduced the earlier found difference of 0.18 e Å^{-3}. The largest charge accumulations (0.44 e Å^{-3}) were found close to oxygen and perpendicular to the equatorial bond, *i.e.* above and below the plane containing the OSi_3 moiety. This feature was interpreted as a natural progression of the lone-pair deformation observed around one- and two-coordinate O atoms and hence noted as important for the bonding in stishovite.

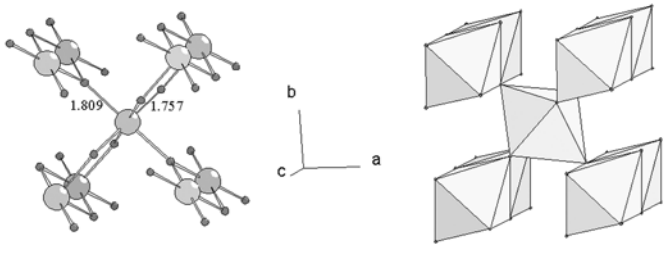

Figure 1
The crystal structure of stishovite viewed along [001]. Left: large spheres Si, small spheres O. The equatorial (1.757 Å) and axial (1.809 Å) Si—O bonds of the SiO_6 coordination 'octahedra' are indicated. Right: chains of edge-sharing 'octahedra' running along [001].

The authors also addressed the nature of the shared-edge ring system characterized by the short Si—Si and O—O contacts of 2.666 (1) and 2.291 (1) Å, respectively, and noted that there were no features that could be interpreted as significant repulsion or attraction between Si atoms, whereas the negative features between next O atoms were rationalized with regard to the Pauli exclusion principle.

A recent X-ray diffraction study by Yamanaka *et al.* (2000) based on effectively 126 reflections measured with Mo $K\alpha$ radiation (s_{max} = 1.2196 Å^{-1}) and ensuing monopole refinements yielded a formal oxygen charge of −1.06 (8) e, in fair agreement with the results obtained by Hill *et al.* (1983). Other results, like the difference density distribution, do not contribute to an improved description of the bond-induced charge redistribution, mainly because the data quality [$R(F) = 0.025$] cannot compete with that of the SHG data.

The present study was prompted by our general interest in silica and silicate structures, by the very successful high-energy (100–150 keV) synchrotron-radiation study of the electron density in cuprite, Cu_2O (Lippmann & Schneider, 2000*a*,*b*), which allowed the determination of essentially absorption- and extinction-free structure amplitudes, and, of course, by the meanwhile available tools for the topological analysis of the total model electron-density distribution (Bader, 1990). Such tools were not developed at the time of the SHG study, and their application is expected to provide more information about the nature of the Si—O bond. In the course of our work, besides measuring new data, we have therefore also used the SHG data, reproduced their results and performed the topological analysis for comparison. Thus, our study aimed at obtaining a new and consistent set of single-crystal data which is unaffected by systematic errors and avoids the problems of merging data from different experiments, as noted by SHG, and at deriving a reliable static density model whose analysis can be carried further by determination of bond critical points (b.c.p.) and associated density properties. With these goals augmented by comparisons between experimental and theoretical band-structure calculation results, we consider our work in line with comparable studies carried out on *e.g.* coesite

Table 1
Crystal data and experimental details.

	Instrument; beamline	
	Four-circle diffractometer; D3	Triple-crystal diffractometer; BW5
Monochromator	Si(111) double-crystal	Si(111) annealed (FWHM = 5.8")
Detector	Plastic scintillation	Ge solid-state
Monitor	Polarimeter	Ring current, scintillation, Si diode
E (keV)	30.995	100.42
λ (Å)	0.400	0.1235
Crystal data		
MW (g)	60.0843	60.0843
F(000) (e)	60	60
a (Å)	4.177 (1)	4.173 (9)
c (Å)	2.6655 (5)	2.657 (4)
Space group	$P4_2/mnm$	
Z	2	
D_x (kg m^{-3})	4.290	
μ (mm^{-1})	0.351	
Transmission	0.932–0.916	
Data collection		
Crystal shape	Irregular, diameter $\simeq$ 0.25 mm	Irregular, diameter $\simeq$ 0.25 mm
s_{max} (Å^{-1}), full sphere	1.539	1.350
Scan mode (continuous)	ω scan	ω scan
Steps	61	61
$\Delta\omega$ (°)	0.025	0.02
Time per step (s)	0.1–0.6	1.0
Standards	222; 404 every 45 min	400 every 60 min
N(refl.)	5951	3795
N(unique)	408	269
$R_{int}(F^2)$	0.04	0.012

(Downs, 1995), danburite (Downs & Swope, 1992), topaz (Ivanov *et al.*, 1998), spodumene (Kuntzinger & Ghermani, 1999) and fibrous zeolites (Kuntzinger *et al.*, 1998; Kirfel & Gibbs, 2000). In the latter reference, the topological results for 32 Si—O, 24 Al—O, 14 Ca—O and 12 Na—O unique bonds were compiled and analysed in terms of both mean values and correlations between bond lengths, oxygen-bonded radii, b.c.p. densities [$\rho(\mathbf{r}_c)$], curvatures at the b.c.p. parallel (λ_3) and perpendicular ($\lambda_{1,2}$) to the bond, Laplacian [$-\nabla^2\rho(\mathbf{r}_c)$] and cation electronegativities. In spite of a relatively wide scatter of the individual bond results, most of the observed trends were found significant and conforming with chemical expectation and with the correlations obtained from model calculations of geometry-optimized molecules (Gibbs *et al.*, 1997; Gibbs, Boisen *et al.*, 1998). Since the distances for the Si—O bonds were confined to values between 1.599 and 1.645 Å, the inclusion of results for sixfold-coordinated Si could be expected to provide more evidence on a considerably wider bond-distance scale.

2. Experimental

The sample material was kindly provided by J. Mosenfelder, Bayerisches Geoforschungszentrum, Bayreuth, Germany. The synthesis was achieved by compressing a Corning grade G silica glass cylinder to 14 GPa, quickly raising the temperature to 1573 K, and holding these conditions for 10 h in a multi-anvil press (6/8 type). The sample was contained in an Re capsule placed in a pressure assembly (MgO octahedron and $LaCrO_3$ furnace). After quenching, a few large single crystals of irregular shapes and dimensions up to 0.3 mm were found in the transformed sample material, two of which with maximum dimensions of 0.25 mm were selected for two different room-temperature diffraction experiments with synchrotron radiation of different wavelengths. Both data collections were carried out at HASYLAB, Hamburg, Germany; details are summarized in Table 1:

(i) Crystal I was investigated on the four-circle diffractometer installed at the bending-magnet beamline D3 using a wavelength of 0.40 Å provided by an Si(111) double-crystal monochromator. A combined intensity/polarization monitor allowed real-time monitoring of both intensity and polarization of the primary beam (for other instrumental details, see *e.g.* Kirfel & Eichhorn, 1990). Intensities were recorded with a plastic scintillation detector with linear response up to 700000 counts s^{-1}. In ω-scan mode, 61 steps of $\Delta\omega = 0.025°$, a full sphere of reflections up to $s_{max} = 1.539$ Å^{-1} was measured resulting in a set of 5951 observations, which, after merging, yielded 408 unique reflections with an internal agreement index $R_{int}(F^2) = 0.04$.

(ii) The data for crystal II were collected on the triple-crystal diffractometer (Bouchard *et al.*, 1998; Lippmann & Schneider, 2000*a*) installed at the high-field wiggler beamline BW5 using a short wavelength of 0.1235 Å produced by an annealed Si(111) single-crystal monochromator. In contrast to D3, the scattering plane is horizontal. The diffractometer components (monochromator, slits, Eulerian cradle, detector *etc.*) run on rails which are mounted approximately perpendicular to the beam and on top of a granite plate so that a variable sample–detector distance has to be corrected for in the course of the data reduction. The reflection intensities were measured using a Ge solid-state detector, and strong count rates exceeding 40000 counts s^{-1} were reduced by calibrated iron absorbers of ascending thicknesses. The data were monitored alternatively using the count rates of a scintillation detector, an Si diode or the DORIS III storage-ring current. The fact that between these monitor modes no significant intensity differences were found can be taken as an indication of the very stable conditions at the beamline. Again in ω-scan mode, 61 steps of $\Delta\omega = 0.020°$, a full sphere of reflections up to $s_{max} = 1.350$ Å^{-1} was measured, the limiting factor being the available beam time. Merging this data set of 3795 observations yielded 269 unique reflections and very satisfactory internal agreement of $R_{int}(F^2) = 0.012$.

The data reductions for both sets, D3 and BW5, were carried out using the program *REDUCE* (Eichhorn, 1987). In the case of BW5, the non-monitored linear polarization of the primary beam was assumed constant and estimated as 90%, based on earlier results reported by Poulsen & Neuefeind (1995) and Vincze (1997). Considering the estimated maximum and minimum transmissions of sample D3 (0.932–0.916), absorption corrections were considered unnecessary for both data sets.

Finally, in the course of the data inspection it turned out that crystal I (D3) exhibited many split reflection peak profiles indicating a domain crystal for which it is possible that occasionally domains remained unexcited in the course of the ω scans. This finding can explain the somewhat disappointing internal consistency of the D3 data, whose quality must therefore be considered as not optimal. Without a detailed inspection of the affected reflections and omitting none of them, we have, however, used them in most calculations for comparison. In the following, however, the discussion is mainly focused on the BW5 data for which profile splitting was encountered in only a few cases.

3. Structure refinements

The structure refinements on the data sets D3 and BW5 using both IAM and GSF models were performed using the program package *VALRAY96* (Stewart *et al.*, 2000), which includes the option for topological analysis of the total model electron density distribution. For a third data set, SHG, the original reflection data reported by Hill *et al.* (1983) and Spackman *et al.* (1987) were combined as described in the latter contribution in order to obtain additional b.c.p. information. All refinements were based on the following:

(i) Structure amplitudes $|F|$.

(ii) Reflection weights $w = [\sigma(F)]^{-2}$ where, for the BW5 data, $\sigma(F)$ is calculated from both counting statistics and an internal consistency factor $p = 0.01$. For the D3 data, $\sigma(F)$ was calculated from the scatter of symmetry-equivalent reflections.

(iii) Reflections with $|F| > 3\sigma(F)$ and no $w\Delta F$ exclusion criterion.

(iv) Neutral atoms using canonical wave functions (Stewart & Spackman, 1983; Clementi, 1965).

(v) Anomalous dispersion corrections taken from Sasaki (1989).

(vi) 'Block mode', *i.e.* different types of variables like crystallographic standard parameters or multipole populations were refined in subsequent cycles, prior to a final full-matrix refinement.

(vii) First derivatives for the normal equations (test calculations including second derivatives failed to yield significant parameter changes).

Initial IAM refinements with variable isotropic extinction correction (Becker & Coppens, 1974*a*,*b*) showed that the high-energy data were free of extinction [$R(F) = 0.0097$], whereas the D3 reflections measured at $\lambda = 0.4$ Å [$R(F) = 0.0115$] were still slightly affected, the largest extinction correction on F^2 being 0.944 for reflection 220. The quality of both data sets was also assessed by high-order refinements (HO, $s_{\min} = 0.7$ Å^{-1}). These converged at $R(F) = 0.0060$ for BW5 and at 0.0090 for D3 (for $s_{\max} = 1.35$ and 1.539 Å^{-1}, respectively). Details of the refinements are given in Table 2.

Table 2
Agreement indices of IAM and GSF refinements.

N(obs.) = number of reflections. N(par.) = number of variables.

Data/model	N(obs.)	N(par.)	$R(F)$	$wR(F)$	GoF
SHG/MOD3	211	26	0.0075	0.0064	1.18
D3/IAM	408	9	0.0115	0.0241	1.35
D3/IAMHO-0.7	363	9	0.0090	0.0239	1.09
D3/MOD3	405	27	0.0086	0.0176	0.99
BW5/IAM	269	8	0.0097	0.0115	2.56
BW5/IAMHO-0.7	222	8	0.0060	0.0048	0.85
BW5/MOD3	269	27	0.0054	0.0043	0.89
BW5/MOD4	269	41	0.0047	0.0038	0.78
BW5/MOD5	269	34	0.0047	0.0038	0.78

Extending the analysis to GSF refinements, various multipole models of different flexibility were tested. Common to the finally used stable models were three monopole populations: PCR for the free neutral atom and PVL and PSH for the valence shells, all constrained to ensure crystal neutrality. In MOD1 with multipoles up to fourth order, all radial functions of the type $r^n \exp(-\alpha r)$ for the individual multipole orders l were assigned a common value α, as earlier performed by SHG. The powers of r for $l = 0$, 2, 4 for the Si atom were $n = 6$, 4, 4, and for $l = 0$–4 for the O atom were $n = 6$, 2, 2, 3, 4. MOD3 features a separately refined expansion coefficient $\alpha(0)$ for the valence shell which turned out to yield a significant model improvement. After convergence at $R(F) = 0.0086$ and 0.0054 for D3 and BW5, respectively, the latter data were additionally used in an extended model MOD4 with multipoles up to seventh order ($n = l$). This model was finally changed into MOD5 by excluding all insignificantly refined multipole populations [POP < σ(POP)] and thus restricting the number of variables. Compared with MOD3, this extension to higher multipole orders led to the inclusion of only seven more significant populations and resulted in a model improvement beyond the 99.995% confidence level according to a Hamilton test (Hamilton, 1965). The final R values obtained for BW5 were $R(F) = 0.0047$, $R_w(F) = 0.0038$, GoF = 0.78, but with respect to deformation density mapping there are hardly any differences between MOD5 and MOD3. An illustration of the excellent agreement between the observed and calculated structure amplitudes on an absolute scale is given in Fig. 2, showing that even very small structure amplitudes below the 1 e margin are well modelled, with relative differences not exceeding 17%.

The crystallographic standard parameters obtained from the refinements on D3 and BW5 are compiled in Table 3 along with the results for the SHG data using MOD3. The differences between BW5/MOD3 and BW5/MOD5 are negligible. Those between D3/MOD3 and BW5/MOD3 are small and may be attributed to both the inferior quality of the D3 data and the still present extinction which seems to cause slightly decreased u_{11} and increased u_{33} for both atoms. Considering

that the two measurements were carried out on different instruments at different wavelengths and on different crystals, however, we regard the mutual agreement of the atomic displacement parameters as a satisfactory indication that none of the data sets are compromised by systematic errors. Larger differences are obtained for the SHG data. Compared with BW5/MOD5, all u_{jj} are increased by the same amount, 25×10^{-5} Å^2, whereas the originally reported SHG parameters reproduced by MOD1 are about 18×10^{-5} Å^2 larger. These increases can be attributed to the different origin of the sample material, to the difference between MOD1 and MOD5, and again to extinction which is most pronounced in the SHG case.

Table 3 contains, in addition, the final radial expansion coefficients for the PVL monopole and the other multipoles, respectively, and the atomic net charges calculated from the adjusted monopole populations. For the Si atom, the mutual agreements for the refined $\alpha(0)$ and α values are within the sums of the respective e.s.d. values, and the averages over the synchrotron results given in Table 3, $\langle\alpha(0)\rangle = 4.4$ (2) and $\langle\alpha\rangle = 1.9$ (1) au^{-1}, conform with the SHG results, $\langle\alpha(0)\rangle = 3.7$ (1.0) and $\langle\alpha\rangle = 2.0$ (2) a.u.$^{-1}$. SHG/MOD1, which corresponds to the model used by SHG, yielded $\alpha = 2.0$ (1) a.u.$^{-1}$, a value which is considerably lower than the standard molecular value of 3.50 a.u.$^{-1}$, in agreement with $\alpha = 2.2$ (1) a.u.$^{-1}$ reported by SHG. In the case of oxygen, $\alpha = 4.3$ (4) a.u.$^{-1}$ obtained from SHG/MOD1 also compares well with the original SHG result [$\alpha = 4.5$ (5) a.u.$^{-1}$] and the standard value of 4.50 a.u.$^{-1}$. When using the more flexible models for the synchrotron data, however, the mean $\langle\alpha(0)\rangle$ is reduced to 2.64 a.u.$^{-1}$ (with large uncertainty), and also $\langle\alpha\rangle$ obtains lower values when the extinction-free BW5 data are considered.

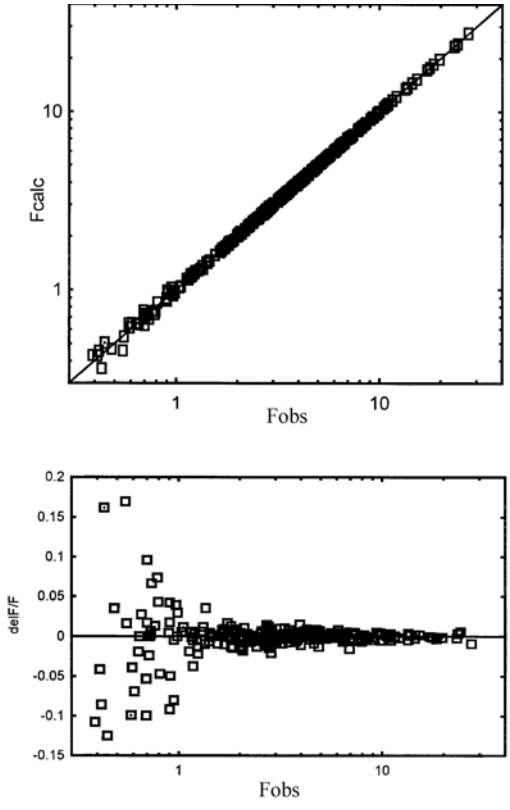

Figure 2
Top: $|F_{calc}|$ *versus* $|F_{obs}|$ on logarithmic scale after BW5/MOD5 refinement. Bottom: relative residuals $\Delta F/|F_{obs}|$ *versus* $|F_{obs}|$.

Table 3
Fractional coordinates, anisotropic displacement parameters (10^5 Å^2), radial expansion coefficients α (a.u.$^{-1}$) and net atomic charges (e) from the monopole populations, with e.s.d. values in parentheses.

Atom		D3/MOD3	BW5/MOD3	BW5/MOD5	SHG/MOD3
Si	u_{11}	211 (1)	219 (1)	218 (1)	243 (2)
	u_{33}	169 (1)	161 (1)	161 (1)	187 (3)
	u_{12}	14 (1)	15 (1)	14 (1)	16 (1)
	$\alpha(0)$	4.2 (2)	4.6 (2)	4.5 (1)	3.7 (1.0)
	α	1.84 (8)	1.98 (8)	1.88 (5)	2.00 (2)
	Q	+2.0 (6)	+1.3 (3)	+2.2 (4)	0.0 (1.2)
O	x	0.30616 (1)	0.30613 (1)	0.30614 (1)	0.30614 (1)
	u_{11}	287 (1)	291 (1)	292 (1)	316 (2)
	u_{33}	231 (1)	220 (2)	218 (2)	242 (4)
	u_{12}	−80 (1)	−85 (1)	−84 (1)	−85 (3)
	$\alpha(0)$	2.9 (7)	2.5 (1.5)	2.5 (9)	5.3 (4)
	α	4.8 (3)	3.5 (2)	3.0 (1)	4.3 (5)
	Q	−1.0	−0.65	−1.1	0.0

Atomic net charges were finally taken from the sums of the refined monopole populations. They clearly indicate the expected charge transfer from Si towards O and conform on average, Q(Si) = +1.83 e, with Q(Si) = +1.71 e given by Hill *et al.* (1983), but the results show considerable uncertainties and their scatter with data and model indicates that a well defined result can hardly be obtained from a single refinement. More meaningful charge values are obtained from spherical charge integrations, $Z(r)$, around the atomic sites. These calculations were carried out by Fourier summations and series truncation error corrections as outlined by Sasaki *et al.* (1980) using the computer program *CHACLI* (Kirfel, 1983). Taking the absolute minima of the radial charge-density distributions, $\partial Z/\partial r$, as defining ionic radii and observing the neutrality constraint, one obtains $Si^{3.25+}O_2^{1.62-}$ and $Si^{2.52+}O_2^{1.26-}$ depending on whether the estimate is based on $\partial Z/\partial r$ of Si or O, respectively. The latter result is close to that derived from the BW5/MOD5 refinement. The charge-transfer question will once more be addressed in §7.

4. Theoretical calculations

Parallel to the evaluation of the experimental data, the electron-density distribution in stishovite was also assessed by theoretical calculations. These were carried out using the *WIEN97* band-structure program (Blaha *et al.*, 1999) using the full-potential linearized-augmented-plane-wave (LAPW) method (Singh, 1994). Based on density functional theory (DFT), the generalized gradient approximation (GGA) of Perdew *et al.* (1996) was used. Data for the lattice constants

and atomic positions were taken from the experimental results. We used radii (Rmt) of 0.82 Å for both the Si and O atomic spheres, a highly converged basis set of up to 1900 LAPWs (using Rmt × Kmax = 11) and 'local orbitals' (LOs) (Singh, 1994) to include Si 2*p* 'semicore' states in the basis. Additional LOs for Si 3*s* and O 2*s*, 2*p* enriched the basis set and reduced any possible linearization error. The density was described by a lattice harmonics expansion up to $L = 8$ inside the atomic spheres and by a Fourier series up to GMAX = 16 in the interstitial regions,

$$\rho(r) = \sum_{LM} \rho(r)_{LM} Y_L^M(r) \qquad \text{for } r < \text{Rmt},$$

$$\rho(r) = \sum_{G} \rho_G \exp(iGr) \qquad \text{for } r > \text{Rmt}.$$

The subsequent topological analysis was performed using a new program (Fuhr & Sofo, 2001) which evaluates the charge density as given by *WIEN97* and analytically calculates gradients from the above expressions (only the radial gradient inside an atomic sphere needs to be calculated numerically). Special care has to be given to the convergence parameters and series truncations, because $\rho(r)$, $\nabla\rho(r)$ and in particular $\nabla^2\rho(r)$ may be discontinuous across an atomic sphere boundary when some expansions are not fully converged or the core electron density fails to vanish at Rmt.

5. Deformation electron density, $\Delta\rho$

For the two planes of interest, the static deformation density distributions $\Delta\rho(\mathbf{r})_{\rm stat}$, as derived from direct-space calculations of BW5/MOD5, are depicted in Figs. 3(*a*) and 4(*a*). These distributions are deconvoluted from thermal motion and can therefore be directly compared with the corresponding theoretical distributions in Fig. 5. Associated residual density distributions calculated by Fourier summations up to $s_{\rm max}$ = 0.8 Å^{-1} are given in Figs. 3(*b*) and 4(*b*) in order to illustrate the quality of the GSF fit.

In Figs. 3(*a*) and 3(*b*), the shorter equatorial bond is in the vertical direction and the longer axial bond is in the horizontal direction. Both bonds contain electron-density peaks of 0.39 (8) e Å^{-3} near the O atom so that the difference of 0.17 (7) e Å^{-3} reported by SHG cannot be corroborated as a characteristic feature of the bonding in stishovite and, since the residual densities at the peak positions show that the observations were well modelled, the only apparent difference between the two bonds is a somewhat more diffuse charge accumulation on the equatorial bond. The close equality of the bonds conforms with calculations using near-Hartree–Fock-limit wave functions for the SiO diatomic molecule (McLean & Yoshimine, 1967) which were quoted by SHG and suggest similar $\Delta\rho$ values of 0.36 and 0.32 e Å^{-3} for the equatorial and axial bond, respectively. The observed equality of the peak heights is also in agreement with the theoretical $\Delta\rho(\mathbf{r})_{\rm stat}$ depicted in Fig. 5(*a*), which exhibits almost equal bond peaks of 0.30 and 0.32 e Å^{-3}. Thus, compared with the calculations, the experimental peak heights are somewhat too large, but they are not significantly different, as predicted by theory. A similar quantitative difference with respect to the band-structure calculations is also observed for the charge accu-

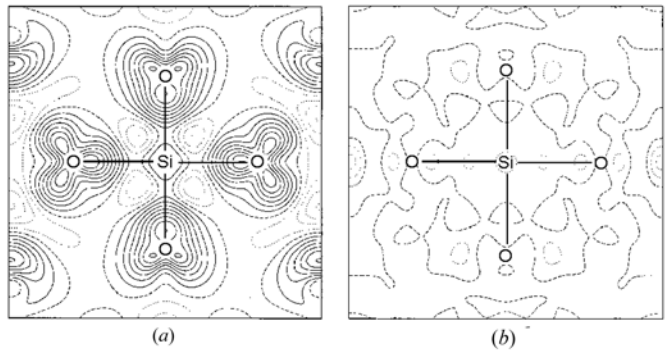

Figure 3
(*a*) Static deformation electron-density distribution $\rho(\mathbf{r})_{\rm stat}$ in the plane through the 'octahedron' (BW5/MOD5). The equatorial bonds are in the vertical direction, the axial bonds in the horizontal direction. Contours at 0.05 e Å^{-3}, zero contour dashed, negative contours dotted. (*b*) Residual electron-density distribution $\Delta\rho(\mathbf{r})_{\rm res}$. Contours as in (*a*).

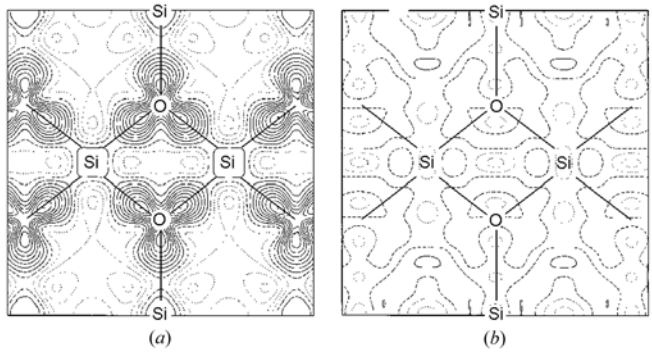

Figure 4
(*a*) Static deformation electron-density distribution $\Delta\rho(\mathbf{r})_{\rm stat}$ in the plane containing the four-membered Si—O—Si—O ring (BW5/MOD5). The shared edge of the 'octahedron' is in the vertical direction. Each O atom shows two equatorial and one axial (vertical) bond. Contours as in Fig. 3(*a*). (*b*) Residual electron-density distribution $\Delta\rho(\mathbf{r})_{\rm res}$, as in Fig. 3(*b*).

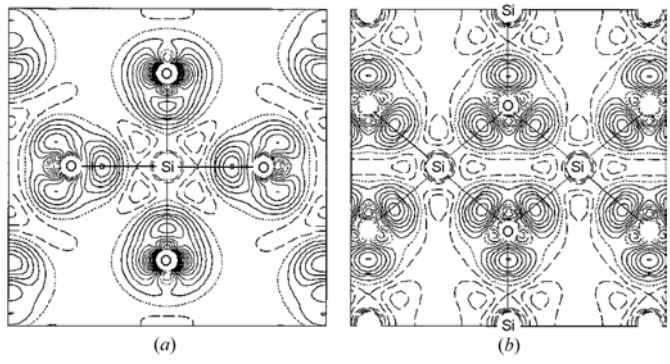

Figure 5
Static deformation electron-density distributions $\Delta\rho(\mathbf{r})_{\rm stat}$ from band-structure calculations (LAPW). (*a*) Section as in Fig. 3(*a*). (*b*) Section as in Fig. 4(*a*). Contours at 0.05 e Å^{-3}, zero contour dashed, negative contours dotted.

mulation perpendicular to the trigonal coordination plane (in Fig. 4) formed by three Si—O bonds which radiate from each O atom. $\Delta\rho$ values for the build up of 'lone-pair' electron density in Fig. 3(*a*) (equatorial bond) are 0.37 (7) e Å^{-3} (X-ray), 0.44 (9) e Å^{-3} reported by SHG and more than 0.5 e Å^{-3} from LAPW. It seems, therefore, that the large difference of 0.34 e Å^{-3} between the axial bond peak and the 'lone-pair' peak obtained by SHG is most likely not a characteristic feature of stishovite, but an artefact caused by some errors in the observed structure amplitudes.

In this study, the only major differences between the experimental and theoretical $\Delta\rho(\mathbf{r})_{\rm stat}$ are found close to the Si and O nuclei where the experimental maps are rather smooth, while the LAPW maps exhibit more pronounced features. This is most probably due to the restricted experimental resolution in $\sin\theta/\lambda$, and the missing features in the experimental maps may also explain why the experimental bond peak maxima are marginally larger and closer to the O nuclei than in theory. Apart from the small differences, however, the overall agreement between the experimental and theoretical $\Delta\rho(\mathbf{r})_{\rm stat}$ is very satisfactory. Not only are the deformations of the oxygen valence shells well reproduced, but also all other density features between the atoms such as the charge depletions around the Si atom pointing towards the coordination 'octahedron' edges or those at the rear of the O atom. This result illustrates the achieved closeness between experiment and theoretical approaches and gives credit to subsequent results of topological analysis.

The same conclusion can be drawn from comparing Figs. 4(*a*) and 5(*b*) which both show the static deformation-density distribution in two adjacent basal planes of Si coordination rhombic dipyramids, defined by the O atoms. The short shared edge is in the vertical direction. These plots illustrate the sp^2-hybridization of the oxygen valence electrons yielding almost equal bond-density peaks at distances of 0.44 Å (experimental) and 0.55 Å (theoretical) from the oxygen nucleus. As for the above-discussed plane running through the 'octahedron', the theoretical features are somewhat less pronounced and the peaks are about 0.1 Å more remote.

Figs. 4(*a*) and 5(*b*) also show, in remarkable agreement, that the interior of the basal plane contains a shallow groove (−0.07 e Å^{-3} in the centre) along the Si—Si direction which can be rationalized by repulsion, mainly between the neighbouring Si atoms. Such charge depletion had already been observed by SHG in difference Fourier calculations, though in the perpendicular direction, but not in the GSF model. Repulsion between adjacent O atoms and their valence electrons is indicated by the asymmetry of the deformation density lobe of the equatorial bond with respect to the Si—O bond direction. In both Figs. 4(*a*) and 5(*b*), the peak maximum is shifted into the larger of the two O—Si—O angles in the basal plane. As a result, the equatorial bond is slightly bent, and it can be expected that, contrary to the axial bond, the bond critical point does not coincide with the straight Si—O connection. Thus, in total, there are no features that could be interpreted as attraction between either Si or O atoms.

6. Total electrostatic potential

As discussed by SHG, the total electrostatic potential can be obtained by combined Fourier summation and direct-space calculations,

$$\varphi(\mathbf{r})_{\rm tot} = \Delta\varphi(\mathbf{r}) + \varphi(\mathbf{r})_{\rm IAM} + \varphi_0,$$

where $\Delta\varphi(\mathbf{r})$ is the deformation electrostatic potential caused by chemical bonding and $\varphi(\mathbf{r})_{\rm IAM}$ is the potential of the procrystal built of free neutral atoms and including the nuclear contributions. The addition of the constant term φ_0 (= −1.376 e Å^{-1} for stishovite) ensures that the mean potential vanishes. Assuming $\varphi(\mathbf{r})_{\rm IAM}$ is error free, the e.s.d. of $\varphi(\mathbf{r})_{\rm tot}$ is that of the Fourier series component which can be separately calculated, values on the Si—O bonds are 0.03 and 0.07 e Å^{-1} outside the octahedron. The interesting planes calculated for BW5/MOD5 are depicted in Figs. 6(*a*) and 6(*b*) and, using the same contour interval of 0.10 e Å^{-1} as SHG, the comparison with Figs. 5(*a*) and 5(*b*) of SHG shows only marginal differences, since the total potential is dominated by the procrystal term. Again, the minimum in the potential in Fig. 6(*a*) is found in the channel between the edge-sharing SiO_6 polyhedra, −1.21 (7) e Å^{-1} (−1.40 e Å^{-1} for D3/MOD3). Both Si—O bonds exhibit similar minima of about −0.10 e Å^{-1} (0.05 e Å^{-1} D3/MOD3), in agreement with SHG. A significant difference occurs in the plane of the shared edges (Fig. 6*b*) where the centre of the four-membered ring Si—O—Si—O exhibits the same potential distribution shape as shown by SHG but with a less deep minimum of −0.53 (3) e Å^{-1} (−0.35 e Å^{-1} D3/MOD3) compared with −0.72 e Å^{-1} taken from Fig. 5(*b*) of SHG. This increase seems to result from the complete absence of extinction, since Spackman & Stewart (1983, 1984) had found an even lower minimum prior to the partial alleviation of the extinction problem by introducing low-order powder data. For the global minimum potential of −0.98 (3) e Å^{-1} (−0.95 e Å^{-1} D3/MOD3) in Fig. 6(*b*), there is again good agreement with SHG [−0.96 (5) e Å^{-1}].

Comparing the X-ray results with the corresponding values from the theoretical calculations, there is also satisfactory agreement. In these latter calculations, the zero potential is

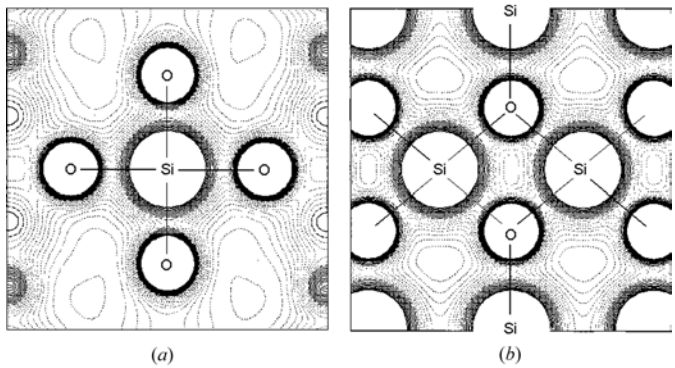

Figure 6
Total electrostatic potential distribution $\varphi(\mathbf{r})_{\rm tot}$ in the planes of Figs. 3(*a*) and 4(*a*). Contours at 0.1 e Å^{-1}, zero contour dashed, negative contours dotted.

Table 4
Bond critical point properties of the Si—O bonds and Si electronegativities obtained from different data and models.

Distances (Å), $\rho(\mathbf{r}_c)$ (e Å^{-3}), $\nabla^2\rho(\mathbf{r}_c)$ and λ_i (e Å^{-5}), e.s.d. values in parentheses. GBHTD estimated from Fig. 2 of Gibbs, Boisen *et al.* (1998).

Data/model	b.c.p. Si	b.c.p. O	$\rho(\mathbf{r}_c)$	$\nabla^2\rho(\mathbf{r}_c)$	λ_1	λ_2	λ_3	ε	χ(Si)
Axial bond (1.809 Å)									
promol (BW5/MOD4)	0.766	1.043	0.618 (1)	6.613 (3)	−1.852 (1)	−1.925 (1)	10.390 (5)	−0.04 (1)	1.597
SHG/MOD1	0.754	1.055	0.694 (4)	4.8 (2)	−3.45 (7)	−3.22 (9)	11.36 (6)	0.04 (4)	1.636
D3/MOD1	0.763	1.046	0.706 (1)	3.60 (8)	−3.61 (6)	−2.41 (2)	9.62 (2)	0.49 (3)	1.646
D3/MOD3	0.757	1.053	0.515 (3)	7.4 (2)	−3.42 (4)	−2.92 (4)	13.70 (5)	0.17 (2)	1.529
BW5/MOD3	0.731	1.077	0.642 (5)	7.7 (1)	−4.45 (7)	−4.28 (8)	16.41 (3)	0.04 (2)	1.600
BW5/MOD4	0.738	1.071	0.604 (6)	8.4 (2)	−4.02 (4)	−3.8 (2)	16.19 (8)	0.06 (5)	1.580
BW5/MOD5	0.738	1.071	0.615 (5)	8.0 (2)	−4.19 (3)	−3.9 (1)	16.08 (6)	0.08 (3)	1.586
Mean	⟨0.747⟩	⟨1.062⟩	⟨0.629⟩	⟨6.64⟩	⟨−3.86⟩	⟨−3.42⟩	⟨13.89⟩	⟨0.14⟩	⟨1.596⟩
LAPW	0.727	1.082	0.656	9.63	−3.97	−3.81	17.42	0.04	1.606
GBHTD		1.08	0.67	9.9	−4.1†		18		1.614
Equatorial bond (1.757 Å)									
promol (BW5/MOD4)	0.743	1.014	0.673 (1)	9.269 (4)	−2.342 (1)	−2.210 (1)	13.821 (6)	0.06 (1)	1.640
SHG/MOD1	0.723	1.036	0.863 (7)	6.7 (2)	−4.9 (1)	−4.52 (9)	16.14 (5)	0.07 (4)	1.728
D3/MOD1	0.729	1.030	0.861 (5)	5.8 (2)	−4.14 (6)	−4.08 (6)	13.99 (2)	0.02 (2)	1.729
D3/MOD3	0.723	1.037	0.721 (5)	8.3 (2)	−5.58 (9)	−4.71 (6)	18.61 (5)	0.19 (2)	1.657
BW5/MOD3	0.711	1.047	0.761 (4)	9.9 (2)	−5.62 (8)	−5.37 (7)	20.90 (3)	0.05 (2)	1.674
BW5/MOD4	0.710	1.047	0.715 (5)	11.9 (2)	−5.67 (8)	−5.1 (1)	22.68 (6)	0.11 (3)	1.651
BW5/MOD5	0.711	1.046	0.710 (4)	12.1 (1)	−5.65 (5)	−4.93 (7)	22.69 (5)	0.14 (2)	1.648
Mean	⟨0.718⟩	⟨1.041⟩	⟨0.772⟩	⟨9.12⟩	⟨−5.25⟩	⟨−4.79⟩	⟨19.16⟩	⟨0.10⟩	⟨1.681⟩
LAPW	0.710	1.047	0.760	11.66	−4.89	−4.72	21.27	0.04	1.674
GBHTD		1.05	0.76	12	−5†		22		1.673

† $\lambda_{1,2}$.

defined by a vanishing average over the potential in the interstitional regions, *i.e.* outside the atomic spheres. This introduces an unknown constant potential shift which was estimated to be −0.14 e Å^{-1} by comparison with the experimental results. Application of this shift to the theoretical potential distribution gives as the minimum potential −1.18 e Å^{-1} in the channel (Fig. 6*a*), about −0.14 e Å^{-1} on the Si—O bonds, −0.56 e Å^{-1} in the centre of the four-membered ring (Fig. 6*b*) and −0.97 e Å^{-1} in the centre of the Si triangle. Thus, most of the electrostatic potential information given by SHG is corroborated by both the experimental determination and the LAPW calculations.

7. Topological analysis

The topological analyses of the total model electron-density distributions $\rho(\mathbf{r})$ obtained from SHG/MOD1, D3/MOD1, D3/MOD3, BW5/MOD3, BW5/MOD4 and BW5/MOD5 were started by checking for positivity throughout an asymmetric unit in the cell. This is an important measure because the GSF model provides no means to guarantee the physically necessary $\rho(\mathbf{r}) \geq 0$ condition. The calculation of $\rho(\mathbf{r})$ carried out for a 0.1 × 0.1 × 0.1 Å grid showed minimum density values of 0.027, 0.030, 0.021, 0.045, 0.012 and 0.012 e Å^{-3}, respectively. Thus, none of the GSF models are compromised by an unphysical negative density value.

The further analyses comprised the calculation of bond critical points (b.c.p.), where the gradient $\nabla\rho(\mathbf{r})$ vanishes (Bader, 1990, 1998), and of associated density properties. These are the density at the b.c.p., $\rho(\mathbf{r}_c)$, the curvatures of the density parallel (λ_3) and perpendicular (λ_1 and λ_2) to the bond, and the ensuing Laplacian, $\nabla^2\rho(\mathbf{r}_c) = \Sigma\lambda_i$, which is the trace of the diagonalized Hessian matrix. If $\nabla^2\rho(\mathbf{r}_c) < 0$ then $\rho(\mathbf{r}_c)$ is locally concentrated; the converse indicates charge depletion. The value of $\rho(\mathbf{r}_c)$ and the magnitude and sign of the Laplacian can be utilized to classify the character of a bond. As stressed by Bader & Essen (1984), a bond qualifies as a shared covalent interaction when $\nabla^2\rho(\mathbf{r}_c)$ is negative and large in magnitude. In contrast, when $\nabla^2\rho(\mathbf{r}_c)$ is positive and large and $\rho(\mathbf{r}_c)$ is relatively small, the bond qualifies as a closed-shell ionic interaction. The b.c.p. properties in stishovite can therefore be used to assess a change of the Si—O bond character, which is intermediate between shared and closed shell, upon changing the Si coordination from four to six.

(3,−1) critical points were found for both Si—O bonds. The distances from the bonded atoms and the b.c.p. properties as obtained for the different data and refinement models are compiled in Table 4 along with corresponding results from the theoretically calculated density distribution (LAPW). The top row contains, in addition, results derived for the procrystal calculated on the basis of the crystallographic standard parameters from BW5/MOD4. These properties may serve to give an impression of the bond-induced redistribution of the electron density.

Considering the b.c.p. positions and the b.c.p. Si and b.c.p. O distances, of which the latter is identical with the oxygen bonded radius R_b(O), Table 4 shows the following:

(i) The b.c.p. positions and hence the atomic-bonded radii vary depending on data and model within at most 0.03 Å.

(ii) The average bonded radii of Si and O are 0.747 Å and 1.062 Å, respectively, for the axial bond and 0.718 Å and 1.041 Å, respectively, for the equatorial bond, and agree within 0.02 Å with theory. If one considers only the BW5

results, this difference reduces further to below 0.01 Å. As already observed for the Si—O bonds in SiO_4 tetrahedra (Gibbs *et al.*, 1992; Feth *et al.*, 1993; Hill *et al.*, 1997; Kirfel & Gibbs, 2000), R_b(O) correlates with the bond length. The shorter the bond, the smaller is the radius of the anion, but at the expense that the cation R_b(O) decreases relatively less than R(SiO). Averaging over the bonds, one finds that the Si radius accounts for 38% of the total bond length; the corresponding value from the spherical charge integrations quoted above is $R_{Si}/(R_{Si} + R_O) = 0.41$. The mean $\langle R_b(O)\rangle = 1.05$ Å is more than 0.1 Å larger than that found for O atoms in SiO_4 units. For these, R_b(O) values are reported as 0.95 Å in coesite (Downs, 1995), 0.92 Å in scolecite (Kuntzinger *et al.*, 1998) or 0.94 Å in natrolite, scolecite and mesolite (Kirfel & Gibbs, 2000). Consequently, the bonded radius for fourfold-coordinated Si is in the range 0.68–0.70 Å and hence not much smaller than that found in this study. Thus, changing at ambient conditions the Si coordination from 4 to 6 results in expansions of both Si and O; however, that of O estimated as +40% is twice as large as that of Si (+20%), both estimates in terms of atomic sphere volumina. In other words, the anion expands at the expense of the cation when the bond distance increases. In this context, it is also interesting to note that the ratio $R_b(Si)/R_b(O) = 0.73$ for four-coordinated Si is larger than 0.70 for stishovite (0.733 procrystal), results that are far from traditional crystal chemical considerations.

(iii) Compared with the procrystal, both b.c.p.s are shifted towards the central Si atom by up to 0.035 and 0.033 Å for the axial and equatorial bond, respectively. These shifts are indications of a charge transfer from Si towards the coordinating O atoms.

(iv) While the b.c.p. on the axial bond coincides with the straight Si—O connection, this is not quite true for the equatorial bond (except for the procrystal), for which the b.c.p. is slightly moved into the larger O—Si—O angle. As a result, the angle subtended at the b.c.p. is 179.4° (BW5/MOD5) or 178.5° (LAPW), conforming with the interpretation of the asymmetric deformation density of the equatorial bond as indicating some strain on the bond. Fig. 7 presents a perspective view of the SiO_6 polyhedron together with neighbouring atoms and the b.c.p.s calculated for BW5/MOD5. The shift of the equatorial b.c.p. is, however, too small to become evident.

Searching for further possible critical points in the structure, the procrystal revealed two (3,+1) points (pales), one at (0,0,0.5) in the centre of the four-membered Si—O—Si—O ring [$\rho(\mathbf{r}_c) = 0.46$ e Å^{-3}, $\nabla^2\rho(\mathbf{r}_c) = 4.12$ e Å^{-5}], the other at (0.2,0.2,0.5) [$\rho(\mathbf{r}_c) = 0.17$ e Å^{-3}, $\nabla^2\rho(\mathbf{r}_c) = 1.57$ e Å^{-5}], approximately in the centre of the triangle defined by three next-neighboured Si atoms. The first pale is retained in both the BW5/MOD5 model electron density [$\rho(\mathbf{r}_c) = 0.365$ (9) e Å^{-3}, $\nabla^2\rho(\mathbf{r}_c) = 5.9$ (3) e Å^{-5}] and, in very good agreement with the experiment, in the theoretical density [LAPW: $\rho(\mathbf{r}_c) = 0.39$ e Å^{-3}, $\nabla^2\rho(\mathbf{r}_c) = 5.6$ e Å^{-5}]. The second pale is also present in theory [$\rho(\mathbf{r}_c) = 0.10$ e Å^{-3}, $\nabla^2\rho(\mathbf{r}_c) = 1.7$ e Å^{-5}], but is not observed in the BW5/MOD5 model density. As indicated in Fig. 7, this density instead exhibited a (3,−1) critical point at (0.22,0.22,0.5) with $\Delta(\mathbf{r}_c) = 0.136$ (5) e Å^{-3}, $\nabla^2\rho(\mathbf{r}_c) = 0.07$ (4) e Å^{-5} and distances of 1.649 Å and 1.865 Å, respectively, from Si. This finding may indicate a very weak metallic interaction between the Si atoms taking place through the face and long basal plane edge of the SiO_6 'octahedron'. In addition to the pale in the centre of the Si—O—Si—O ring, the BW5/MOD5 model density also yielded another (3,−1) critical point at (0,0,0.417) with $\rho(\mathbf{r}_c) = 0.366$ (8) e Å^{-3} and $\nabla^2\rho(\mathbf{r}_c) = 5.0$ (2) e Å^{-5}, which, in view of the density value, compared with that of the adjacent pale may, however, well be an artefact. Thus, bonded interactions across the four-membered ring seem unlikely, in agreement with SHG.

The changes of the outer quantum shells caused by chemical bonding are clearly reflected in the Laplacian which displays the valence-shell charge concentration (VSCC). Relief maps of $+\nabla^2\rho\Delta(\mathbf{r})$ with arbitrary cut-offs of ±20 e Å^{-5} for the *K*- and *L*-shell spikes are given in Fig. 8 for both interesting planes. The positive sign of the Laplacian was chosen for clarity because $\nabla^2\rho(\mathbf{r})$ is positive everywhere between the atoms. This finding is in agreement with the mixed shared and closed-shell nature of the atomic interaction with dominance

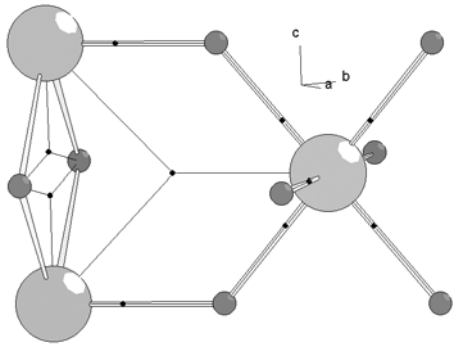

Figure 7
BW5/MOD5: (3,−1) bond critical points (small black spheres) in the SiO_6 'octahedron', the Si—O—Si—O ring at (0,0,0.5) and the Si—Si—Si triangle at (0.22,0.22,0.5) (Si large spheres, O medium spheres). The b.c.p.s of the Si—O bonds obtained from the band-structure calculations coincide with the 'experimental' points.

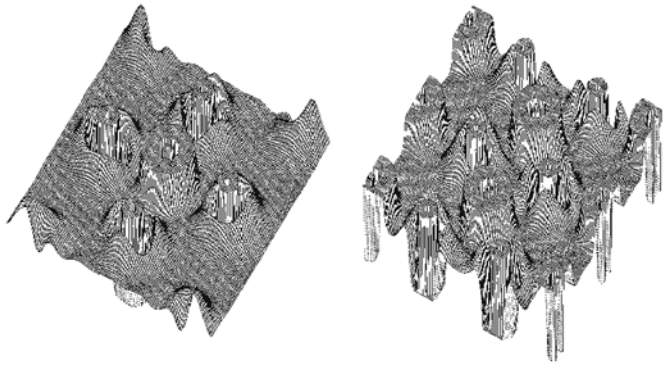

Figure 8
Positive Laplacian distributions $\nabla^2\rho(\mathbf{r})_{stat}$ in the planes of Figs. 3(*a*) and 4(*a*) (BW5/MOD5). The equatorial bond in the left-hand plot is pointing towards the viewer. Spikes are arbitrarily cut at ±20 e Å^{-5}.

of the latter, *i.e.* a great part of the Si valence electrons is transferred to the oxygen whose valence shell is then in turn polarized towards the surrounding cations. The equatorial bond in Fig. 8(*a*) is pointing towards the viewer, and in Fig. 8(*b*) the shared edge is approximately horizontal. As observed for danburite (Downs & Swope, 1992), coesite (Downs, 1995), topaz (Ivanov *et al.*, 1998) and fibrous zeolites (Kirfel & Gibbs, 2000), the VSCC of the oxide anion is well developed, *i.e.* the oxygen valence-electron shell shows a hill structure, while that of the Si atom is poorly developed and diffuse. The hills of up to 16 e Å^{-5} around O indicate regions of charge depletion with their maxima located right between internuclear lines, and the lowest saddle points between these maxima point towards the Si atom, in agreement with an sp^2 hybridization. Both plots emphasize the similarity of the two Si—O bonds, though in agreement with the deformation-density maps the maxima and saddles belonging to the axial bond are somewhat more diffuse.

7.1. B.c.p. properties

By inspection of the b.c.p. properties and comparison of the mean values obtained from the different data sets and models, both similarities and differences are revealed. The individual results exhibit a considerable scatter that is not covered by the calculated e.s.d. values and demonstrates that the b.c.p. properties are model properties that must not be over-interpreted. On the other hand, since three different crystals and diffraction experiments are involved in this analysis, the overall agreement, particularly for the BW5 results, seems satisfactory enough to consider average values. These values, implicitly giving most weight to the BW5 data, whose quality is considered best, should be physically meaningful and sufficient to reveal trends. For practically all quantities, the LAPW data agree very well with these mean values, and often even better agreement is found with the BW5 data indicating again their better quality (a typical example is λ_3 at the axial b.c.p., 17.42 e Å^{-5} in LAPW compared with the mean value of 13.89 e Å^{-5} and 16.22 e Å^{-5}, the average over the BW5 results).

$\rho(\mathbf{r}_c)$ correlates with the bond distance, the shorter bond shows a larger density (0.77 e Å^{-3}) than the longer bond (0.63 e Å^{-3}) and, since both values are larger than the corresponding procrystal densities, charge is concentrated on the bonds. This is supported by the decrease of λ_1 and λ_2, for which the absolute values show the same negative correlation with the bond distance as does $\rho(\mathbf{r}_c)$. The average absolute curvatures, $\lambda_{1,2} = |\lambda_1 + \lambda_2|/2 = 4.97$ e Å^{-5} for the equatorial bond and 3.64 e Å^{-5} for the axial bond, are both smaller than results found for four-coordinated Si (*e.g.* 6.8 e Å^{-5} in danburite, 7.0 e Å^{-5} in coesite) and indicate a decrease of the shared interaction contribution to the bond. Since λ_3 is also found to decrease with increasing bond length, the observed trends conform with those calculated for coesite and $H_{12}Si_5O_{16}$ molecules (Rosso *et al.*, 1999) and found in the fibrous zeolites (Kirfel & Gibbs, 2000).

Comparison can also be made with the b.c.p. properties calculated for 14 hydroxyacid geometry-optimized molecules with Si—O bonds (Gibbs, Boisen *et al.*, 1998). These calculations yielded dependences from the bond distance in a range between 1.5 and 2.0 Å. Extracting for the bond lengths in stishovite from Fig. 2 (Gibbs, Boisen *et al.*, 1998), property values denoted as GBHTD in Table 4, one finds fair agreement with the mean values of Table 4 which improves further if only the BW5 results are considered. This is also illustrated in Fig. 9, which shows the data points taken from Table 1 of Gibbs, Boisen *et al.* (1998) fitted with a second-order polynomial as a guide for the eyes. The additional square symbols represent mean values for natrolite, scolecite and mesolite taken from Kirfel & Gibbs (2000) and the averages of the BW5 results taken from Table 4 of this study.

With our new results, which extend the experimentally covered range of Si—O distances, all the correlations evaluated by Gibbs, Boisen *et al.* (1998) are corroborated, both qualitatively and quantitatively. Thus, their description of the Si—O bond is supported, according to which there is a progressive build-up of electron density at $\mathbf{r}_c$ with decreasing bond length. The charge accumulation is accompanied by increasing curvatures of the density at $\mathbf{r}_c$ both perpendicular and parallel to the bond. Increases of density and curvature perpendicular to the bond are consistent with an increasing shared interaction as the bond distance decreases. The increasing covalent component is also reflected in the ellipticities, $\varepsilon = (\lambda_1/\lambda_2 - 1)$, at least for those obtained for BW5 where ε increases from 0.06 to 0.10 for the equatorial bond and hence indicates an increasing π contribution to the bond. Conversely, both the curvature parallel to the bond and the Laplacian decrease with decreasing bond length, which would be consistent with an increasing closed-shell interaction. As already discussed by Gibbs, Boisen *et al.* (1998), this result conflicts with the Bader & Essen (1984) criteria, but similar correlations were also obtained in model calculations for Ge—O bonds and other oxide and nitride molecules containing first- and second-row cations (Hill *et al.*, 1997; Feth *et al.*, 1998).

7.2. Electronegativity and b.c.p. properties

The last column in Table 4 contains Si electronegativities estimated by the expression (Boyd & Edgecombe, 1988; Hill *et al.*, 1997)

$$\chi = 1.31\{R_b(\mathrm{O})/[N\rho(\mathbf{r}_c)]\}^{-0.23},$$

where N is the number of valence electrons of the cation, *i.e.* four for Si. This correlation has been found to yield χ values for the cation that agree to within some percent with Pauling's thermochemical electronegativities, and it introduces χ as a bond-specific property. The values given in Table 4 are considerably lower than Pauling's 1.80 for Si. They indicate an increasing electronegativity difference with increasing distance between Si and O and hence increasing closed-shell interaction for the bond. Simultaneously, it is evident that the

χ estimate for Si in the procrystal is hardly changed by the chemical bonding, *i.e.* owing to the inherent correlation between the anion-bonded radius [R_b(O)] and $\rho(\mathbf{r}_c)$ the procrystal itself already provides a reasonable estimate of bond-specific electronegativities. Correlations between χ and bond distance, $\rho(\mathbf{r}_c)$, $\lambda_{1,2}$ and λ_3 are plotted in Fig. 10. As for Fig. 9, these plots contain the stishovite results in comparison with molecular model values calculated from the b.c.p. properties given in Table 1 of Gibbs, Boisen *et al.* (1998) together with experimental mean values obtained for the fibrous zeolites (Kirfel & Gibbs, 2000). There is close agreement for χ *versus* R(Si—O) and $\rho(\mathbf{r}_c)$, respectively, and a satisfactory agreement for χ *versus* the curvatures, which are not at all used in the χ estimates. Thus, also with respect to the electronegativity, the experimental results for stishovite are consistent with the picture that the change from four- to six-coordinated Si is accompanied by an increase in Si—O bond length, decreases of the percentage *s* character of the hybrid orbitals and the electronegativity and hence an increase of the closed-shell interaction character of the bond. In fact, using Pauling's (1940) estimate the ionicity of the bond increases from about 51% to 58%.

7.3. Atomic charges and volumina

Space partitioning into atomic basins for Si and O can be achieved by analysing the gradient vector field of the total model charge-density distribution. These basins are defined by surfaces which are not crossed by gradient vectors, *i.e.* the 'zero flux' criterion $\nabla\rho(\mathbf{r})\cdot\mathbf{n}(\mathbf{r}) = 0$ holds for each surface point, where $\mathbf{n}(\mathbf{r})$ is the surface normal vector (Bader, 1990). With the space partitioning algorithm implemented in *VALRAY* (Flensburg & Madsen, 2000), the calculations for the determination of the boundaries of the gradient field were carried out on the basis of $6 \times 6 \times 6$ unit cells and 96 2-planes and 72 radial integration steps yielding 6388 points on the surface. The resulting Si basin (Fig. 11) clearly reflects the octahedral coordination by the O atoms, in spite of the somewhat fringed edges. The much larger O basin exhibits a more irregular form, for which the next contacts with Si are indicated by arrows. Subsequent charge integrations over the Si and O basins served to determine the numbers of electrons contained and hence atomic charges. Table 5 summarizes the independently (*i.e.* without constraints) obtained charge results, the individual atomic basin volumina and equivalent

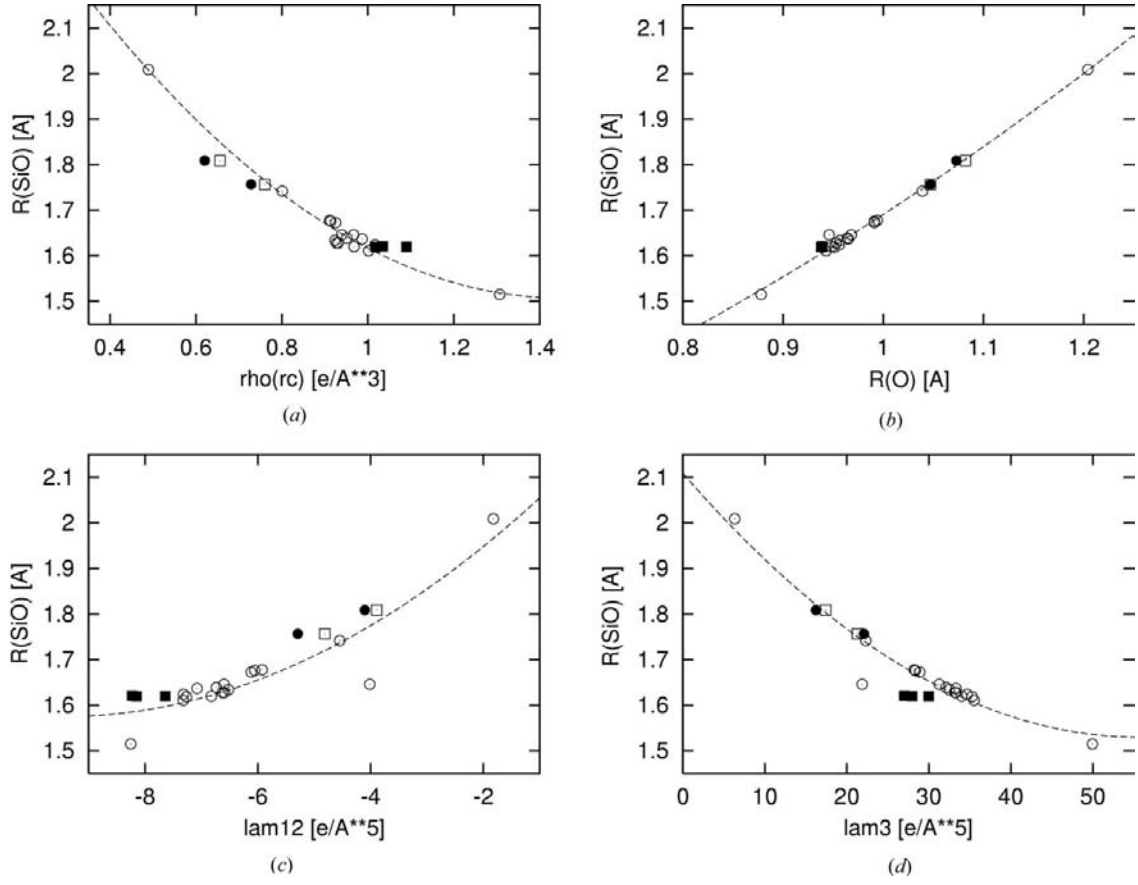

Figure 9
Correlations between Si—O bond lengths and b.c.p. properties. Open circles are taken from geometry-optimized molecule calculations (Gibbs, Boisen *et al.*, 1998), full squares are taken from fibrous zeolites (Kirfel & Gibbs, 2000), full circles indicate experimental (Table 4) and open squares indicate LAPW results of this study. (*a*) R(SiO) *versus* bond critical point density $\rho(\mathbf{r}_c)$. (*b*) R(SiO) *versus* oxygen bonded radius R_b(O). (*c*) R(SiO) *versus* mean curvatures perpendicular to the Si—O bonds λ_{12}. (*d*) R(SiO) *versus* curvatures parallel to the Si—O bonds λ_3.

Table 5
Atomic charges Q (e), volumina V (Å^3) and equivalent sphere radii r (Å) obtained from 'atomic basin' calculations.

V_{cell} = 4651 Å^3.

Data/model	Q(Si)	Q(O)	$Q(SiO_2)$	V(Si)	V(O)	$2V(SiO_2)$	r_{eq}(Si)	r_{eq}(O)
promol (BW5/MOD4)	+2.44	−1.22	0.0	4.42	9.44	46.60	1.02	1.31
SHG/MOD1	+2.90	−1.46	0.02	3.17	10.06	46.58	0.911	1.340
D3/MOD3	+3.32	−1.66	0.0	2.60	10.35	46.60	0.853	1.352
BW5/MOD3	+3.36	−1.68	0.0	2.40	10.44	46.56	0.831	1.355
BW5/MOD4	+3.39	−1.69	0.01	2.30	10.47	46.50	0.820	1.357
BW5/MOD5	+3.39	−1.69	0.01	2.30	10.47	46.50	0.820	1.357
LAPW	+3.30	−1.65	0.0					
Natrolite	⟨+3.44⟩	⟨−1.66⟩						
Mesolite	⟨+3.24⟩	⟨−1.40⟩						
Scolecite	⟨+3.14⟩	⟨−1.52⟩						

radii of ion spheres, and $Q(SiO_2)$ as well as $2V(SiO_2)$ as indicators of the quality of the basin determination. For correct partitioning, $Q(SiO_2)$ should vanish and $2V(SiO_2)$ should equal V_{cell}. Since space partitioning was also carried out for the theoretical density (LAPW), corresponding results are included in Table 5, and, for comparison, charge results for fourfold-coordinate Si in fibrous zeolites (Waasmaier, 1997) are also added.

Considering the atomic basin volumina and the resulting $2V(SiO_2)$, it is evident that the space partitioning worked well. Compared with the unit-cell volume of 46.51 Å^3, $2V(SiO_2)$ differs at most by 0.19% and only by 0.02% for BW5/MOD5. Correct partitioning and scaling are also indicated by $Q(SiO_2)$, which is less than 0.02 e in all cases. Differences in atomic volumina and associated charge values can therefore be ascribed to the models, but not to the algorithm.

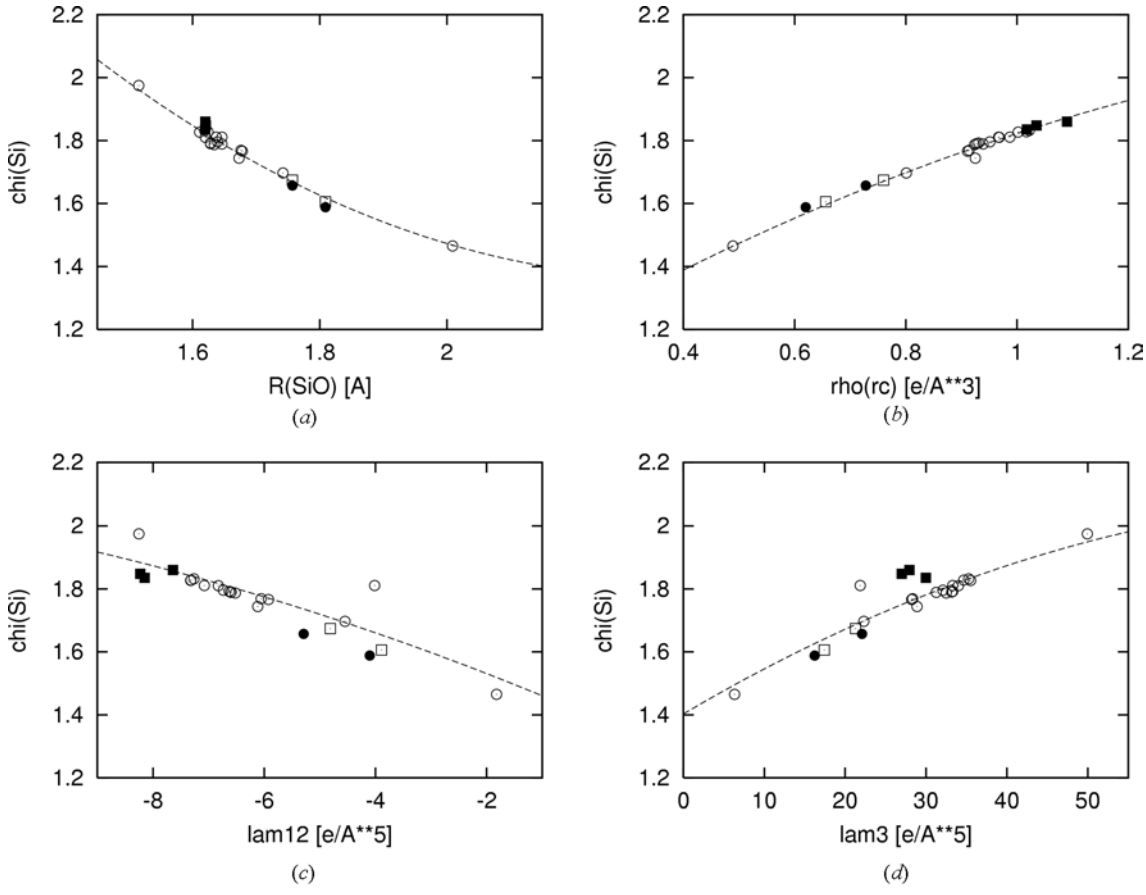

Figure 10
Correlations between Si electronegativity χ(Si) and b.c.p. properties. Symbols as in Fig. 9. (*a*) χ(Si) *versus* Si—O bond lengths. (*b*) χ(Si) *versus* bond critical point density $\rho(\mathbf{r}_c)$. (*c*) χ(Si) *versus* mean curvatures perpendicular to the Si—O bonds λ_{12}. (*d*) χ(Si) *versus* curvatures parallel to the Si—O bonds λ_3.

The comparison of V(Si) and V(O) in the procrystal with the volumina of the bonded species shows that the bonding and the concomitant charge transfer leads to significant volume changes, particularly for Si. Expressed by the equivalent radii r_{eq}(Si) and r_{eq}(O), the oxygen radius increases by about 3.6% at the expense of the Si atom, whose radius decreases by 20%. It is interesting to note that the bonded r_{eq}(O) is very close to the effective ionic radius (IR) of the three-coordinate O^{2-} anion, IR = 1.36 Å (Shannon, 1976). Consequently, IR(Si) = 0.40 Å is much smaller than r_{eq}(Si) = 0.82 Å. The ionic radii obtained from the spherical charge integrations (see §3), r(Si) = 0.83 Å and r(O) = 1.345 Å, are, on the other hand, close to r_{eq}(Si) and r_{eq}(O). These radii, derived from the respective radial charge distributions, yield atomic volumina V(Si) = 2.395 Å^3 and V(O) = 10.19 Å^3, both in fair agreement with the topological analysis results, though V(O) is somewhat underestimated. Hence, it is worth noting that the spherical charge integration is still a reasonable method for estimating atomic volumina from conventional IAM structure refinements.

With the exception of the least flexible SHG/MOD1, all charge results indicate a large charge transfer from Si towards O, which conforms with the notion of a predominantly closed-shell interaction inferred from the b.c.p. properties. This is also strongly supported by the transfer derived from the band-structure calculation (LAPW), for which the difference of only 2.6% signifies a very satisfactory agreement between the theoretical and experimental results. With the obtained charges, Q(Si) = +(3.30–3.39) e, Q(O) = −(1.65–1.69) e, both atoms reach 82.5–85% of full ionization. Comparing this finding with Q(Si) from the Fourier charge integration, Q(Si) = +3.25 e, one can again conclude that this method yields reasonable charge estimates, whereas, in agreement with Lippmann & Schneider (2000*b*), the values derived from the monopole populations of the GSF models (Table 3) are generally too small.

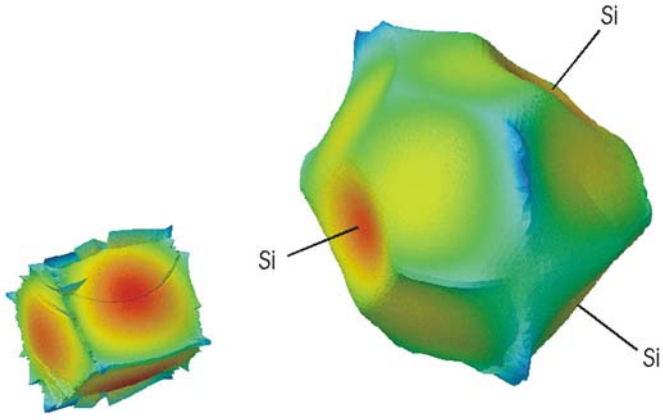

Figure 11
Surface plots of the atomic basins of Si (left) and adjacent oxygen (right) on the same scale. Next O—Si contacts are indicated by rules.

Unfortunately, it is not yet possible to compare the results of Table 5 with corresponding data for four-coordinate Si in coesite, since space partitioning was not performed in the study by Downs (1995). The only data available to our knowledge are mean charges for the fibrous zeolites taken from Waasmaier (1997), who also calculated atomic basins using *VALRAY*. These data indicate similar charge transfers between Si and O, but a direct comparison is difficult due to the presence of Na^+ and Ca^{2+} cations which polarize the O atoms. In fact, from natrolite *via* the intermediate mesolite to scolecite, the order of decreasing charge attraction, according to the different cation electronegativities, is clearly reflected in the mean SiO charge transfers. Nevertheless, the similarity of the results reported in Table 5 supports the usefulness of space partitioning in assessing electrostatic properties of bonded atoms and emphasizes the achieved coherence to date between experimental and theoretical electron-density studies.

8. Conclusions and summary

The present study augments and completes a detailed investigation of the electron-density distribution in the geophysically and mineralogically relevant stishovite structure, having been started by Hill *et al.* (1983) and continued by Spackman *et al.* (1987). Besides re-evaluating these data and reproducing the results, new single-crystal data were collected using medium- and high-energy synchrotron radiation, *i.e.* at wavelengths of 0.40 and 0.1235 Å, respectively, in order to obtain internally consistent data sets exhibiting little or no extinction effects. While the first data were still not completely free of extinction, this fully applied to the high-energy data measured at a wiggler beamline. Both data sets were evaluated by generalized scattering factor structure model refinements, yielding agreement indices well below the 0.01 margin, and ensuing calculations of direct-space properties and topological analyses of the model electron-density distributions. Since it turned out that the quality of the high-energy data was significantly better than that of the 0.40 Å data, the density analysis was focused on the former measurements. As found in a comparable density study on cuprite (Lippmann & Schneider, 2000*a*,*b*), the high-energy synchrotron data are well suited for the determination of a reliable density model and its subsequent topological analysis from both of which details of the electrostatic properties and chemical bonding were derived. The experimental study was accompanied by a theoretical band-structure calculation using the LAPW method. The resulting electron density distribution was also topologically analysed in order to allow for a mutual comparison of theory and experiment.

Already from the respective static deformation density distributions it is evident that the total density distributions obtained by both GSF modelling of the experimental data and theoretical band-structure calculations agree well, in spite of the non-identical (IAM) reference systems. Not only are the general density features along the Si—O bonds very similar, but also are the details of the density in non-bonding inter-

nuclear regions. Remarkable differences occur only in the vicinities of the nuclei, but such differences are naturally due to both the limited resolution of the experimental data and the limited flexibility of the refinement model as required by large parameter correlations. Thus, the good overall agreement can be considered as strong support for the quality of the total charge-density description achieved with the high-energy experiment and *vice versa* for the validity of the theoretical approach.

The deformation densities obtained from both methods show that the two different Si—O bonds are essentially equal in character. They possess significant shared-interaction components and simultaneously exhibit reasonable quantitative differences with respect to the positions of and the total density properties at the bond critical points. These b.c.p. properties associated with about 10% longer Si—O bonds, as compared with those produced by fourfold-coordinated Si, add new information to the experimental evidence of the nature of the Si—O bond obtained so far. In particular, they are well conforming with the correlations between bond length and b.c.p. properties derived from model calculations of geometry-optimized molecules (Gibbs, Boisen *et al.*, 1998). The general picture that is supported by the new observations shows that, as R(SiO) gradually increases in value, the density, the curvature along the bond and the Laplacian at the critical point decrease, while the oxygen bonded radius and the mean curvature perpendicular to the bond increase. Thus, with increasing bond length, in spite of decreasing λ_3, electron density is progressively lowered at $\mathbf{r}_c$, corresponding to a decrease in the shared-interaction component, or, in other words, with increasing bond length the bond with predominantly closed-shell interaction character gains further in ionicity. This is also clearly reflected in the trends obtained for the bond-specific cation electronegativity which decreases as the bond becomes longer and the density and the absolute curvatures decrease at $\mathbf{r}_c$. Such a decrease enhances the electronegativity difference between the bonding partners and hence increases the ionicity of the bond. For stishovite, the increase associated with the change of the Si coordination from 4 to 6 is estimated as about 7%. In agreement with these findings, the atomic electron numbers obtained by direct-space partitioning according to the zero-flux criterion indicate a large charge transfer corresponding to 82.5% (band-structure calculation) to 85% (experiment) ionization of the atoms. In this context, it is noteworthy that for both experimental and theoretical density distributions the independently calculated atomic basin volumina and numbers of electrons contained therein summed up for two formula units yield results which are very close to $V_{\rm cell}$ and $F(000)$, respectively, and thus give credit to the quality of the analysis. It should also be noted that a well comparable 81% ionization is obtained from the simple spherical charge integration by Fourier summation method when the absolute minimum of the Si radial charge distribution function is considered, and that the topologically analysed procrystal density distribution already yields 61% ionization, merely due to the localized superposition of the free-atom density distributions. The comparison of these results with the significantly smaller atomic charge estimates following from the monopole populations emphasizes that charge values and ensuing classifications of bonds can only be reasonably related if derived by the same method.

References

Bader, R. F. W. (1990). *Atoms in Molecules.* Oxford: Oxford Science.
Bader, R. F. W. (1998). *J. Phys. Chem.* **102**A, 7314–7323.
Bader, R. F. W. & Essen, H. (1984). *J. Chem. Phys.* **80**, 1943–1960.
Becker, P. J. & Coppens, P. (1974*a*). *Acta Cryst.* A**30**, 129–147.
Becker, P. J. & Coppens, P. (1974*b*). *Acta Cryst.* A**30**, 148–153.
Blaha, P., Schwarz, K. & Luitz, J. (1999). *Wien97* (K. Schwarz, TU Wien, ISBN 3-9501031-0-4). Improved version of Blaha, P., Schwarz, K., Sorantin, P. & Trickey, S. B. (1990). *Comput. Phys. Commun.* **59**, 399–415.
Bouchard, R., Hupfeld, D. & Lippmann, T. (1998). *J. Synchrotron Rad.* **5**, 90–101.
Boyd, R. J. & Edgecombe, K. G. (1988). *J. Am. Chem. Soc.* **110**, 4182–4186.
Chao, E. C., Fahey, J. J., Littler, J. & Milton, E. (1962). *J. Geophys. Res.* **67**, 419–421.
Clementi, E. (1965). *IBM J. Res. Dev.* **9** (Suppl.).
Downs, J. W. (1995). *J. Phys. Chem.* **99**, 6849–6956.
Downs, J. W. & Swope, J. R. (1992). *J. Phys. Chem.* **96**, 4834–4840.
Eichhorn, K. (1987). *REDUCE. Program for Data Reduction of Step-Scan Measured Reflection Profiles for Both Neutrons and X-rays.* HASYLAB/DESY, Hamburg, Germany. (Unpublished.)
Feth, S., Gibbs, G. V. & Boisen, M. B. Jr (1993). *J. Phys. Chem.* **97**, 11445–11450.
Feth, S., Gibbs, G. V., Boisen, M. B. Jr & Hill, F. C. (1998). *Phys. Chem. Miner.* **25**, 234–241.
Flensburg, C. & Madsen, D. (2000). *Acta Cryst.* A**56**, 24–28.
Fuhr, J. & Sofo, J. (2001). To be published.
Gibbs, G. V. (1982). *Am. Mineral.* **67**, 421–450.
Gibbs, G. V., Boisen, M. B. Jr, Hill, F. C., Tamada, O. & Downs, R. T. (1998). *Phys. Chem. Miner.* **25**, 574–584.
Gibbs, G. V., Hill, F. C. & Boisen, M. B. Jr (1997). *Phys. Chem. Miner.* **24**, 167–178.
Gibbs, G. V., Spackman, M. A. & Boisen, M. B. Jr (1992). *Am. Mineral.* **77**, 741–750.
Hamilton, W. C. (1965). *Acta Cryst.* **18**, 502–510.
Hill, F. C., Gibbs, G. V. & Boisen, M. B. Jr (1997). *Phys. Chem. Miner.* **24**, 582–596.
Hill, R. J., Newton, M. D. & Gibbs, G. V. (1983). *J. Solid State Chem.* **47**, 185–200.
International Tables for X-ray Crystallography (1974). Vol IV. Birmingham: Kynoch Press (Present distributor: Kluwer Academic Publishers, Dordrecht.)
Ivanov, Y. U., Belokoneva, E. L., Protas, J., Hansen, N. K. & Tsirelson, V. G. (1998). *Acta Cryst.* B**54**, 774–781.
Kirfel, A. (1983). *CHACLI. Program for Spherical Charge Integration by Fourier Summation.* University of Bonn, Germany. (Unpublished.)
Kirfel, A. & Eichhorn, K. (1990). *Acta Cryst.* A**46**, 271–284.
Kirfel, A. & Gibbs, G. V. (2000). *Phys. Chem. Miner.* **27**, 270–284.
Kuntzinger, S. & Ghermani, N. E. (1999). *Acta Cryst.* B**55**, 273–284.
Kuntzinger, S., Ghermani, N. E., Dusausoy, Y. & Lecomte, C. (1998). *Acta Cryst.* B**54**, 819–833.
Lippmann, T. & Schneider, R. J. (2000*a*). *J. Appl. Cryst.* **33**, 156–167.
Lippmann, T. & Schneider, R. J. (2000*b*). *Acta Cryst.* A**56**, 575–584.
McLean, A. D. & Yoshimine, M. (1967). *IBM J. Res. Dev.* **13**(3), 206.
Pauling, L. (1940). *The Nature of the Chemical Bond*, 2nd ed. Cornell University Press.
Perdew, J. P., Burke, S. & Ernzerhof, M. (1996). *Phys. Rev. Lett.* **77**, 3865–3868.

Poulsen, H. & Neuefeind, J. (1995). *Nucl. Instrum. Methods*, B**95**, 509–514.
Reid, A. F. & Ringwood, A. E. (1969). *J. Solid State Chem.* **1**, 6–9.
Ringwood, A. E. (1967). *Earth Planet. Sci. Lett.* **2**, 255–263.
Ringwood, A. E., Reid, A. F. & Wadsley, A. D. (1967). *Acta Cryst.* **23**, 1093–1095.
Rosso, K. M., Gibbs, G. V. & Boisen, M. B. Jr (1999). *Phys. Chem. Miner.* **26**, 264–272.
Sasaki, S. (1989). *Numerical Tables of Anomalous Scattering Factors Calculated by the Cromer and Liberman's Method.* KEK Report 88–141, pp. 1–45. KEK, Tsukuba, Japan.
Sasaki, S., Fujino, K., Takeuchi, Y. & Sadanaga, R. (1980). *Acta Cryst.* A**36**, 904–915.
Shannon, R. D. (1976). *Acta Cryst.* A**32**, 751–767.
Singh, D. (1994). *Plane Waves. Pseudopotentials and the LAPW Method.* Dordrecht: Kluwer.
Spackman, M. A., Hill, R. J. & Gibbs, G. V. (1987). *Phys. Chem. Miner.* **14**, 139–150.
Spackman, M. A. & Stewart, R. F. (1983). *American Crystallography Association, Program and Abstracts*, Vol. 11, No. 1. Abstract L1.
Spackman, M. A. & Stewart, R. F. (1984). *Methods and Applications in Crystallographic Computing*, edited by S. R. Hall & T. Ashida, pp 302–320. Oxford University Press.
Stewart, R. F. & Spackman, M. A. (1983). *VALRAY User's Manual.* Carnegie Mellon University, Pittsburgh, PA, USA.
Stewart, R. F., Spackman, M. A. & Flensburg, C. (2000). *VALRAY User's Manual*, Version 2.1. Carnegie Mellon University, Pittsburgh, PA, USA, and University of Copenhagen, Denmark.
Stishov, S. M. & Popova, S. V. (1961). *Geochemistry*, **10**, 923–926. (Engl. transl.)
Vincze, L. (1997). Private communication.
Waasmaier, D. (1997). Thesis, University of Würzburg, Germany.
Yagi, T., Mao, H. K. & Bell, P. M. (1978). *Phys. Chem. Miner.* **3**, 97–110.
Yamanaka, T., Kurashima, R. & Mimaki, J. (2000). *Z. Kristallogr.* **215**, 424–428.